Applied Catalysis B: Environmental 179 (2015) 178–184

Contents lists available at ScienceDirect

Applied Catalysis B: Environmental

journal homepage: www.elsevier.com/locate/apcatb

Pd@Pt core–shell nanostructures for improved electrocatalytic activity in methanol oxidation reaction

Young-Woo Lee[a,b,1], Jin-Yeon Lee[a,1], Da-Hee Kwak[a], Eui-Tak Hwang[a], Jung Inn Sohn[b], Kyung-Won Park[a,*]

[a] Department of Chemical Engineering, Soongsil University, Seoul 156-743, Republic of Korea
[b] Department of Engineering Science, University of Oxford, Oxford OX1 3PJ, United Kingdom

ARTICLE INFO

Article history:
Received 19 November 2014
Received in revised form 31 March 2015
Accepted 12 May 2015
Available online 14 May 2015

Keywords:
Platinum
Palladium
Cube
Core shell
Methanol oxidation reaction

ABSTRACT

The core–shell nanostructures are developed as a way to improve the specific mass activity of the catalyst for the methanol electrooxidation reaction. We prepared the shape-controlled Pd@Pt core–shell nanoparticles using a seeding method with hetero-nucleation process in the presence of PVP. The as-prepared Pd@Pt core–shell nanoparticles consist of a well-defined core–shell structure with a Pd core and Pt shell, cubic shape exposed {100} facets, ~97% yield, and approximately 2.5 nm thickness of Pt shell. The cubic Pd@Pt nanoparticles exhibit remarkably improved electrochemical properties *i.e.*, improved specific mass current density and more negative potential of the forward peak for methanol electrooxidation in comparison with pure cubic Pt and commercial Pt electrocatalysts.

1. Introduction

Direct methanol fuel cells (DMFCs) as low-temperature fuel cells have been intensively investigated as a promising power source for portable electronic devices and fuel cell vehicles [1–3]. For anode catalyst in DMFCs, the Pt electrodes have been well known as the most effective catalysts for methanol electrooxidation reaction in acid electrolyte [4–7]. However, despite the high efficiency, polycrystalline Pt catalyst has exhibited critical problems such as high cost and low specific mass and/or area electrochemical activity [8–10]. To solve these problems, the critical factors affecting the electrocatalytic properties of Pt electrocatalysts are identified as the control of surface structure, alloy, and the core–shell of the nanostructure catalysts [11–13].

Pt-based catalysts with shape- and structure-controlled nanostructures have exhibited significantly the enhanced catalytic reaction rates over those of polycrystalline Pt, which can be expected to have a high specific catalytic activity. Interestingly, Pt {100} facet exhibits higher electrocatalytic activity and different selectivity than Pt {111} facet, for methanol electrooxidation reaction in acid electrolyte [14]. Because of the highly specific area for electrocatalytic activity of {100} facets, the cubic Pt nanostructures mainly including the exposed {100} facets have been reported by many research studies on the methanol electrooxidation reaction [15,16]. It was reported that the Pt-based alloy nanoboxes and nanocubes consisting of dominant {100} facets are synthesized by chemical reduction in organic based solution, which could improve methanol oxidation in comparison with the polycrystalline Pt catalysts [17,18].

Alternatively, for the reduced Pt loading amount, the critical factors are alloy, core–shell, bi-functional support, *etc.* [19–21]. In DMFCs, the loading amount of Pt catalysts is an important factor, because it is immediately correlated with the unit cost of fuel cell manufacturing. Among these structures, the core–shell nanostructures were developed as a way to improve the specific mass activity of the catalyst over those of pure metallic materials, which is directly associated with the unit cost of fuel cell manufacturing. Thus, for the improved specific mass electrochemical activity, the core–shell nanostructures should have the exposed surface structures of platinum atoms and the thin layer of shell structures in core–shell nanoparticles (NPs) [22,23]. In the recent paper, Kuai et al. reported that the gold–platinum yolk-shell structure was synthesized using a galvanic displacement method, and it exhibited the highest electrochemical mass activity which accounted for approximately 4 times higher electrochemical mass activity than Pt nanoparticles in methanol electrooxidation reaction [24].

* Corresponding author. Tel.: +82 2 820 0613; fax: +82 2 812 5378.
E-mail address: kwpark@ssu.ac.kr (K.-W. Park).
[1] These authors contributed equally to this work.

http://dx.doi.org/10.1016/j.apcatb.2015.05.029
0926-3373/

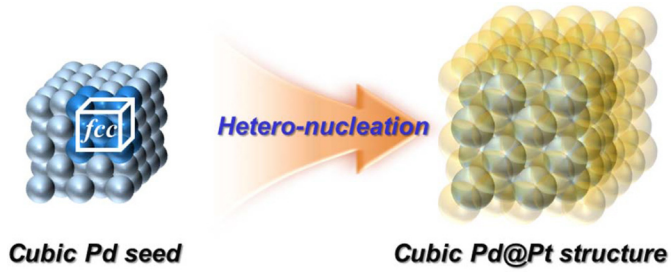

Fig. 1. Schematic illustration of synthesis process of the cubic Pd@Pt NPs by a seeding method with hetero-nucleation.

For metallic nanostructures with improved specific area/mass electrochemical activity, there have been many efforts to manipulate the structure-controlled NPs by using various synthesis methods [15,18,24]. For structure-controlled metallic NPs, the polyol and thermal-decomposition methods are well-known as the most attractive methods, and they have many advantages such as having a facile synthesis approach as well as uniform and homogeneous size and shape [24–27]. In particular, these synthesis methods consist of surfactant- and/or solution-based synthesis, which might be prepared by using colloid-type production and a high distribution of NPs for the production on a large scale, in comparison with the electrochemical and photochemical reduction methods.

Herein, we synthesized the Pd@Pt core–shell NPs for methanol electrooxidation using a thermal decomposition method and polyol method in the presence of poly(vinyl pyrrolidone) (PVP) in comparison with pure cubic Pt and polycrystalline Pt electrocatalysts. For the synthesis of Pd@Pt core–shell NPs, we selected a seeding method *via* the heterogeneous nucleation process. The synthesis approach is illustrated in Fig. 1. The cubic Pd NPs, as core and seed materials, were synthesized by a selective binding of Br^- ion on Pd {100} facets [28,29]. The cubic Pd@Pt core–shell NPs were achieved using a heterogeneous nucleation process with cubic Pd NPs as seeds. The structural and chemical characterizations of the pure Pt cubes and Pd@Pt core–shell NPs were analyzed by field-emission transmission electron microscopy (FE-TEM), X-ray diffraction (XRD) analysis, energy dispersive X-ray (EDX) spectroscopy, and X-ray photoelectron spectroscopy (XPS). Also, the elemental compositions of Pt and Pd in the as-prepared cubic Pd@Pt core–shell catalysts were measured using inductively coupled plasma mass spectrometer (ICP-MS). The electrochemical properties of the as-prepared electrocatalysts were measured and compared using a potentiostat.

2. Experimental

2.1. Synthesis of cubic Pd@Pt NPs

The cubic Pd NPs as core material were prepared by reducing the Pd salt in aqueous solution. The 0.0294 g of sodium tetrachloropalladate (Na_2PdCl_4, 6 mM, Aldrich), 0.088 g of NULL-ascorbic acid ($C_6H_8O_6$, 10 mM, Aldrich), 0.3 g of sodium bromide (NaBr, 20 mM, Aldrich), and 0.105 g of PVP (MW = 29,000, Aldrich) were mixed with continuous stirring in 50 mL of H_2O. The mixed solution was kept at 100 °C for 3 h under constant mixing until the Pd salts were completely reduced. The resulting black colloid solution with the Pd NPs was cooled down to 25 °C. The product was precipitated by centrifugation and washed several times with acetone, ethanol, and deionized water to remove the PVP as a capping agent. The Pd naoparticles were dispersed in 5 mL of H_2O. For the cubic Pd@Pt core–shell NPs, the 25 mL of chloroplatinic acid hexahydrate (2 mM $H_2PtCl_6{\cdot}6H_2O$, Aldrich), 0.053 g of NULL-ascorbic acid, 0.133 g of PVP, and 5 mL of cubic Pd seed were despersed in H_2O and mixed with continuous stirring in 20 mL of H_2O. The mixed solution was kept at 80 °C for 2 h until the Pt salts were completely reduced. The resulting colloid solution with Pd@Pt core–shell NPs was cooled down to 25 °C. The product was precipitated by centrifugation and washed several times with acetone, ethanol, and deionized water to remove the PVP as a capping agent. The Pd@Pt core–shell NPs were dispersed in 5 mL of H_2O.

2.2. Synthesis of cubic Pt NPs

In our previous study, we prepared the cubic Pt nanostructure using a thermal decomposition method [15]. The cubic Pt nanostructures were prepared by reducing Pt salt in an organic-based solution. For the solution of dissolved platinum acetylacetonate salt ($Pt(acac)_2$, Aldrich), the 5 mL of 1-octadecene solution containing 2 mM $Pt(acac)_2$ and 25 mg of PVP was prepared in a 30 mL vial. On the other hand, the 10.78 mL 1-octadecene ($C_{18}H_{36}$, Aldrich) solution containing 9.22 mL of oleylamine ($C_{18}H_{37}N$, Aldrich), 12.6 mg of oxalic acid ($C_2H_2O_4{\cdot}2H_2O$, Johnson Matthey Co.), and 25 mg of PVP was prepared in a three-neck flask (50 mL) under a nitrogen atmosphere. The dissolved Pt salt solution with yellow color was injected into a heated solvent with continuous stirring. The solution was kept for 2 h at 250 °C until the Pt salts were completely reduced under nitrogen atmosphere.

2.3. Structural and electrochemical analysis

For the structural analysis of the catalysts, XRD analysis was carried out using a Rigaku X-ray diffractometer with Cu Kα (λ = 0.15418 nm) source and a Ni filter. The source was operated at 40 kV and 100 mA. For all of the XRD measurements, the resolution in the scans was kept at 0.02°. The morphology and size of the catalysts were characterized by FE-TEM using a Tecnai G2 F30 system operating at 300 kV. The TEM samples were prepared by placing drops of catalyst suspension dispersed in ethanol on a carbon-coated copper grid. The energy dispersive X-ray analysis of the catalysts was performed on a field emission transmission electron microscope. Also, the elemental compositions of Pt and Pd in the as-prepared cubic Pd@Pt core–shell catalysts were measured using ICP-MS (ELAN 6100, PerkinElmer). X-ray photoelectron spectroscopy (XPS) (Thermo Scientific, K-Alpha) analysis was carried out using an Al Kα X-ray source of 1486.8 eV at a chamber pressure below 1×10^{-8} Torr and beam power of 200 W. The electrochemical properties of the catalysts were measured in a three-electrode cell at 25 °C, using a potentiostat (Eco Chemie, AUTOLAB). Pt wire and Ag/AgCl (in saturated KCl) were used as a counter and reference electrode, respectively. The catalyst ink was prepared by ultrasonically dispersing the catalyst powders in an appropriate amount of Millipore water, 5 wt% Nafion® solution (Aldrich), and 2-propanol solution (C_3H_8O, Sigma). The catalyst ink was dropped onto a glassy carbon working electrode (area ~0.0706 cm^2). After drying in an overn at 50 °C oven, the metallic loading amount of the as-prepared catalysts was 40 μg cm^{-2}. To compare the electrocatalytic properties of the catalysts, cyclic voltammograms (CVs) were obtained between −0.2–+1.0 V in an Ar-saturated 0.1 M $HClO_4$ solution with a scan rate of 50 mV s^{-1} at 25 °C. To evaluate the electrocatalytic activities of the as-prepared catalysts, CVs were obtained between −0.2–+1.0 V in an Ar-saturated 0.1 M $HClO_4$ + 2.0 M CH_3OH with a scan rate of 50 mV $^{-1}$ at 25 °C, respectively. Also, for comparison of electrocatalytic stability, the as-prepared electrocatalysts were kept at 0.45 V for 7200 s in Ar-purged 0.1 M $HClO_4$ containing 2.0 M CH_3OH. To compare electrochemical properties, the Pt/C catalyst (20 wt% Pt deposited on Vulcan XC-72, E-TEK, Co.) was used.

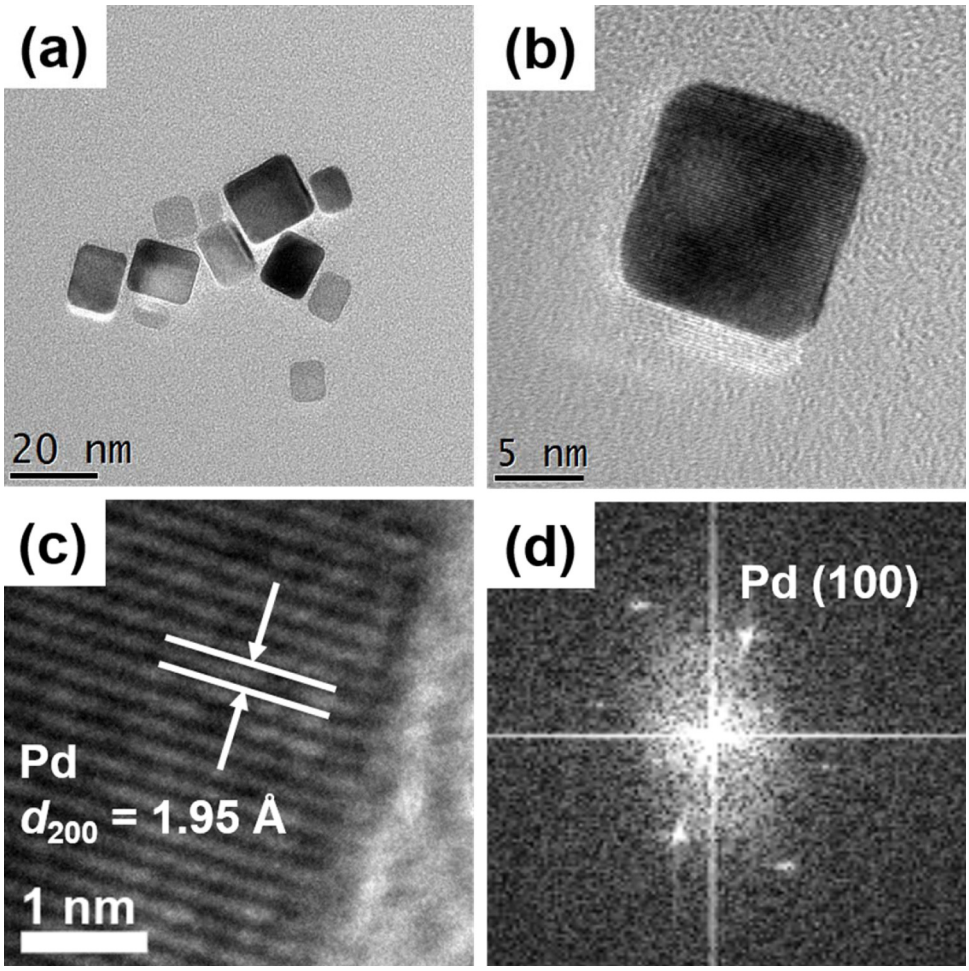

Fig. 2. (a) TEM and (b) HR-TEM images of the cubic Pd NPs. (c) HR-TEM image of a single cubic PdNP containing {100} facets. (d) the FFT pattern of the cubic Pd NPs in Fig. 2(c).(For interpretation of the references to color in this figure legend, the reader is referred to the web version of this article.)

3. Results and discussion

For seeding materials, we synthesized the cubic Pd NPs by reducing Pd salts with L-ascorbic acid and sodium bromide in an aqueous solution at low temperature. Fig. 2shows a TEM image of the as-synthesized Pd NPs as core materials. The Pd NPs exhibit an average particle size of 23 nm and ~92% yield of cubic shape (denoted as cubic Pd NPs), as shown in Fig. 2(a and b). The cubic Pd NPs represent the {100} facets with d-spacing of 0.195 nm of the Pd metallic phase based on a face-centered-cubic (fcc) crystal structure, as shown in Fig. 2(c). The fast Fourier transform (FFT) pattern indicates that the Pd nanocube is a single crystal with its surface enclosed by {100} facets, as shown in Fig. 2(d). In the present synthesis process, it is expected that the Br^- ions as a capping agent can lead to anisotropic growth of the cubic nanocrystal, which is driven by selective chemisorption of the Br^- ion on {100} facets of the Pd crystal. Lim et al. reported that the Br^- ions as capping agent can be easily synthesized on Pd nanocubes due to their preferential chemisorption and monolayer adsorption on the {100} facets of Pd crystal [30,31].

The cubic Pd@Pt core–shell NPs (denoted as cubic Pd@Pt NPs) were synthesized by a seeding method consisting of heterogeneous nucleation growth of the Pt on the as-prepared cubic Pd NPs as core material. Fig. 3(a) and (b) show TEM images of the as-synthesized Pd@Pt NPs with uniform and homogenous cubic shape, which contains an average particle size of 25.5 nm and ~97% yield of cubic shape. Fig. 3(c) shows a high-angle annular dark-field scanning TEM (HAADF-STEM) image of cubic Pd@Pt NP, consisting of Pt shell as relatively lighter region and Pd core as relatively darker region. This outcome is consistent with the cubic Pd@Pt core@shell nanostructure. Also, to identify the elemental distribution of the cubic Pd@Pt NP, EDX elemental mapping images were obtained, as shown in Fig. 3(d). It is evident that the cubic Pd@Pt NPs contain Pt (green) in the core and Pd (red) in the shell. Furthermore, the Pt shell on the cubic Pd@Pt NP has the homogeneous Pt atoms deposited on Pd {100} facets, with approximately 1.25 nm of shell thickness.

In particular, as shown in Fig. 4 the HR-TEM image of a single cubic Pd@Pt NP shows a continuous epitaxy from the Pd as a core to Pt as the shell. In the shell area, the Pt represents the {100} facets with d-spacing of 0.198 nm of the Pt metallic phase based on a face-centered-cubic (fcc) structure, as shown in Fig. 4(b). On the other hand, in the core region, the d-spacing is measured to be 0.195 nm of the {100} facets in the Pd metallic phase, which means that the cubic Pd NP exists as a core material. Also, the measurements of the FFT pattern in Fig. 4(b) and (c) are in agreement with the proposed core–shell structure, in that the distance from the center to the spot of (200) plane slightly increases. Thus, this implies that the cubic Pd@Pt NPs show epitaxy growth *via* heterogeneous nucleation, which formed a well-defined core–shell structure with their surface enclosed by {100} facets. Also, as confirmed by the EDX, the cubic Pd@Pt NPs are element components consisting of 77.5 at% of Pd and 22.5 at% of Pt. Furthermore, as confirmed by ICP-MS, the elemental compositions of Pd and Pt in the as-prepared cubic Pd@Pt NPs are 75.2 and 24.8 at%, respectively. By compar-

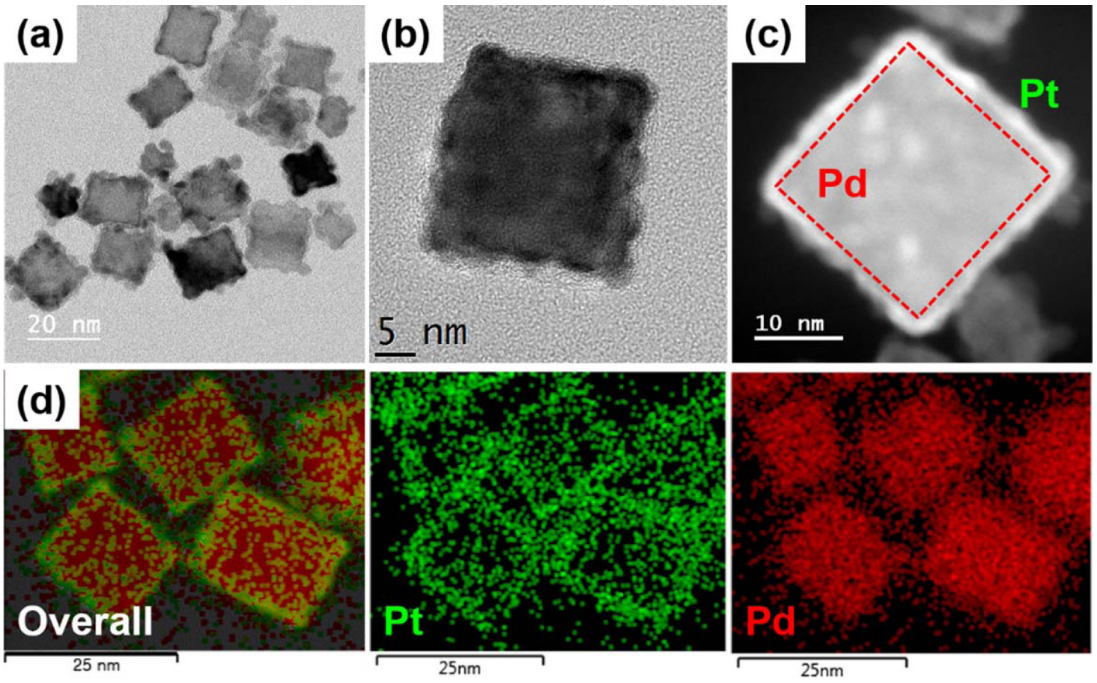

Fig. 3. (a) TEM and (b) HR-TEM images of the cubic Pd@Pt NPs. (c) HAADF image of a single cubic Pd@Pt NP. (d) EDX element mapping images for the Pt (green) and Pd (red).(For interpretation of the references to color in this figure legend, the reader is referred to the web version of this article.)

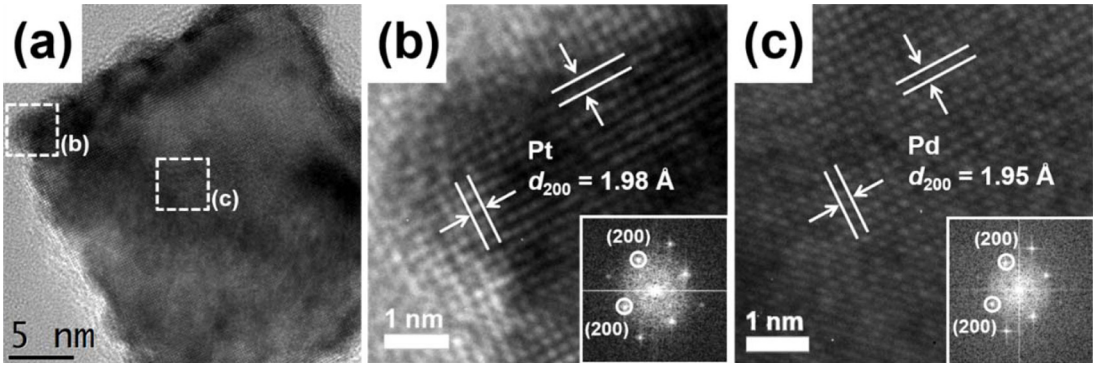

Fig. 4. (a) HR-TEM image of a single cubic Pd@Pt NP. (b) HR-TEM image of the Pt shell region of the cubic Pd@Pt NP. The inset indicates a FFT pattern of the Pt shell region. (c) HR-TEM image of the Pd core region of the cubic Pd@Pt NP. The inset indicates a FFT pattern of the Pd core region.

ing EDX and ICP-MS data, it can be concluded that the as-prepared cubic Pd@Pt NPs are a well-defined elemental composition in the core–shell nanostructures. Furthermore, the surface chemical state and composition of individual components in the as-prepared NPs were obtained by XPS (Fig. S1). In the case of the cubic Pd@Pt NPs, the Pt $4f_{7/2}$ peak consists of metallic and oxide states, *i.e.*, the peaks for Pt^0, Pt^{2+}, and Pt^{2+} at ~71.5, ~72.5, and ~74.4 eV, respectively, and the corresponding composition of surface state is ~67.6, ~18, and ~14.3. Contrastively, the Pd $3d_{5/2}$ peak only consists of metallic state (~335.7 eV). The XPS peaks of Pd and Pt are slightly shifted from the pure Pd and Pt, which can be attributed to the change of electronic structures by interface interaction between Pd and Pt [32].

Fig. 5 shows the XRD pattern of the cubic Pd@Pt NPs in comparison with the XRD reference data of Pt (red, JCPDS No. 04-0802) and Pd (blue, JCPDS No. 46-1043). In the case of the cubic Pd@Pt NPs, the XRD peaks at 39.93, 46.48, and 67.92 correspond to the (111), (200), and (220) plane, respectively, in an fcc structure. In the case of the core–shell nanostructures, the diffraction peak in the XRD pattern is generally separated according to each metal. However, in the case of the Pd and Pt crystal structures in the core–shell nanostructures, the peaks of Pt and Pd cannot be resolved by the X-ray diffractometer due to the very small lattice mismatch factors (0.77% for Pt/Pd) [32,33]. For the comparison of electrochemical activity of the cubic Pd@Pt NPs in methanol electrooxidation reaction, we synthesized the cubic Pt NPs using a thermal-decomposition method as reported in our previous study [15]. As shown in the TEM images (Fig. 6), the as-prepared Pt NPs appear to have a uniform cubic shape and ~4.5 nm of average size of NPs. The cubic Pt NP is a single crystal with their surface enclosed by {100} facets with d-spacing of 0.19451 nm of Pt metallic phase, as shown in Fig. 6(b).

To identify the electrochemical properties of the catalysts, the hydrogen desorption region curves were obtained in 0.1 M $HClO_4$ with a scan rate of 50 mV s^{-1} at 25 °C, as shown in Fig. 7. The hydrogen desorption curves of the catalysts consist of oxidation peaks at −0.125 V and −0.031 V. Marković et al. and Wang et al. reported that the {100} facets of a Pt crystal surface led to a distinct hydrogen desorption peak between −0.1 and 0.0 V as compared to Ag/AgCl [34,35]. The cubic Pt electrocatalysts exhibit a relatively intense peak at −0.03 V due to the dominantly exposed {100} facets of the cubic Pt NPs as compared to commercial Pt/C (E-TEK, Co.) which has main hydrogen desorption peak at −0.15 V. In particular, the

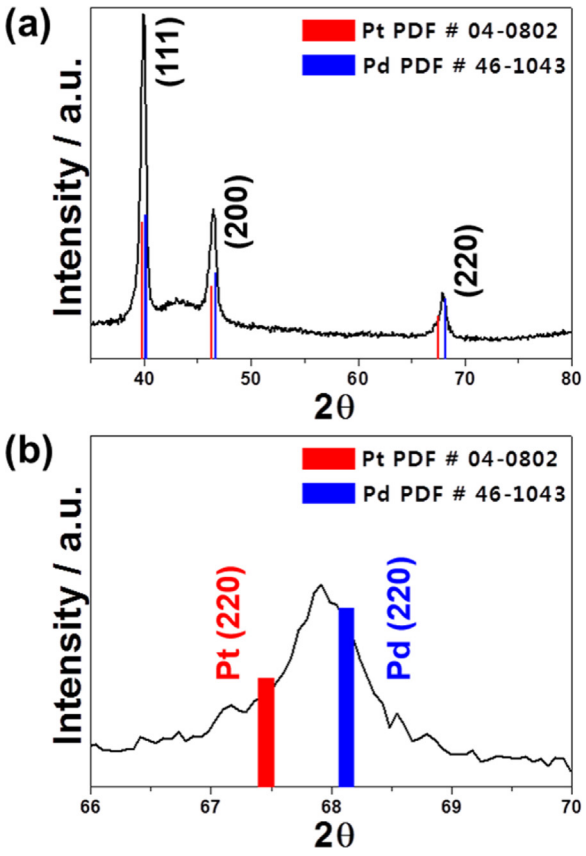

Fig. 5. (a) wide-range XRD pattern of the cubic Pd@PtNPs. (b) The diffraction peak of (2 2 0) plane in the cubic Pd@PtNPs in comparison with the XRD reference data of Pt (red) and Pd (blue).(For interpretation of the references to color in this figure legend, the reader is referred to the web version of this article.)

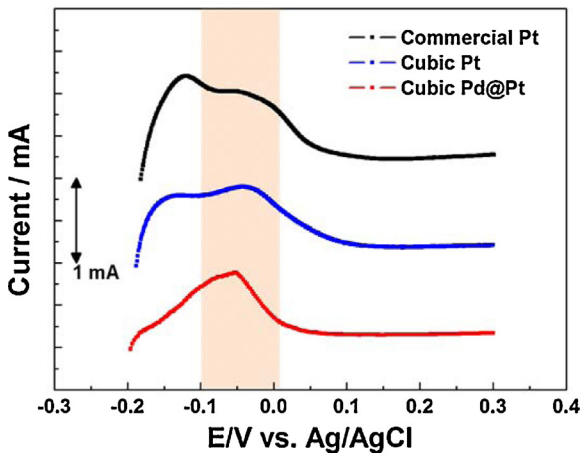

Fig. 7. Hydrogen desorption region curves of cubic Pd@Pt, cubic Pt, and commercialPt electrocatalysts in an Ar-saturated 0.1 M HClO4with a scan rate of 50 mV s^{-1} at 25 °C.

cubic Pd@Pt electrocatalysts show a hydrogen oxidation peak at −0.05 V. This means that the Pt shell in cubic Pd@Pt NPs consists of a well-defined shell formation on the cubic Pd NPs, and a surface enclosed by {100} facets results from the growth along the {100} crystal planes.

To identify the electrochemical properties of the catalysts, CVs were obtained in 0.1 M $HClO_4$ + 2.0 M CH_3OH with a scan rate of 50 mV s^{-1} at 25 °C, as shown in Fig. 8(a). The electrochemical characteristic curves in methanol electrooxidation were normalized by the loading amount of metallic catalysts on the glassy carbon as a working electrode. The negative peak potential of the cubic Pd@Pt electrocatalyst indicates an excellent catalytic activity for methanol electrooxidation in comparison with that of the cubic Pt and commercial Pt electrocatalysts. Manohara et al. suggested that the anodic peak in the reverse scan might be attributed to the removal of the incompletely oxidized intermediate species formed in the forward scan [36]. Hence, the ratio of the forward anodic peak current density (I_f) to the reverse anodic peak current density (I_b), *i.e.*, I_f/I_b, can be used to describe the tolerance of a catalyst to the accumulation of intermediate species during ethanol electrooxidation. The cubic Pd@Pt (1.12) and cubic Pt (1.64) electrocatalysts show ratios of I_f/I_b higher than 0.53 for commercial Pt electrocatalyst. Furthermore, at +0.6 V, the current density of the cubic Pd@Pt electrocatalyst (130.7 A $g^{-1}{}_{metal}$) is higher than that of the cubic Pt (80.7 A $g^{-1}{}_{metal}$) and commercial Pt (47.2 A $g^{-1}{}_{metal}$) electrocatalysts, as shown in Fig. 8(b). The shape-controlled and core–shell nanostructures exhibit less accumulation of residues on the catalyst during methanol oxidation, and thus, an excellent catalytic activity. Moreover, according to the calculation of the specific mass activity by Pt amount, the cubic Pd@Pt electrocatalyst shows 7.2 and 12.3 times higher specific mass current density compared to the cubic Pt and commercial Pt electrocatalysts, respectively, as shown in Fig. 8(c). Furthermore, the specific mass activity of cubic Pd@Pt electrocatalyst (48.7 A $g^{-1}{}_{Pt}$) is 3.45 times higher than that of the commercial Pt electrocatalysts (14.1 A $g^{-1}{}_{Pt}$) at 0.4 V.

Table 1 shows comparison for the electrocatalytic properties of various catalysts for methanol electrooxidation reaction with the cubic Pd@Pt electrocatalyst. The forward peak potential of the cubic Pd@Pt electrocatalyst in methanol electrooxidation reaction

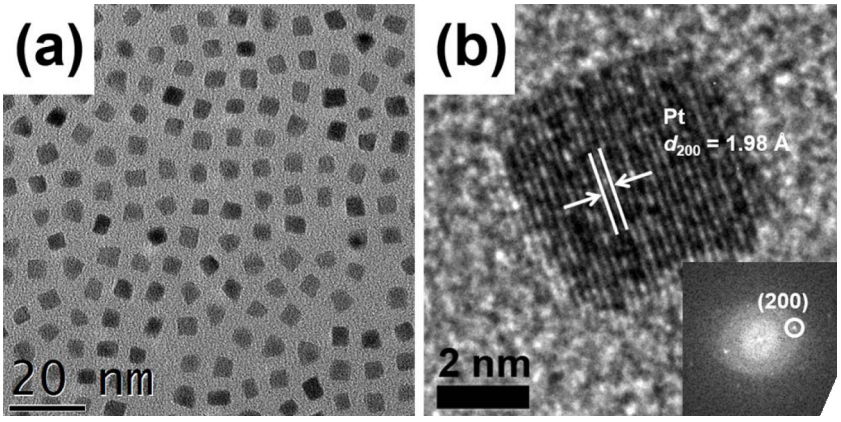

Fig. 6. (a) TEM image of the cubic Pt NPs. (b) HR-TEM image of a single cubic Pt NP. The inset indicates a FFT pattern of the cubic Pt NP.

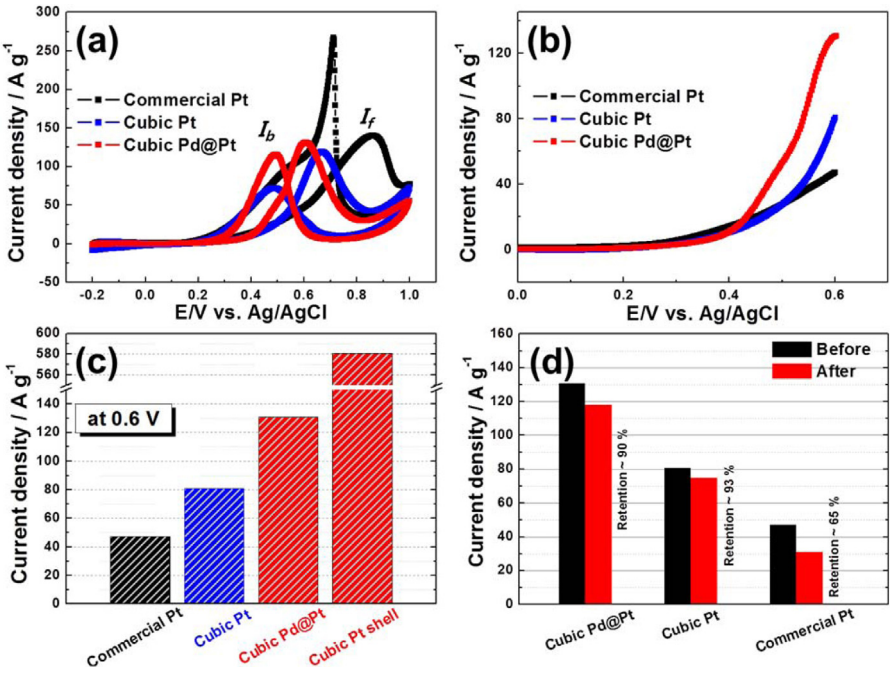

Fig. 8. (a) CVs of cubic Pd@Pt, cubic Pt, and commercial Pt electrocatalysts in 0.1 M $HClO_4$ + 2.0 M CH_3OH with a scan rate of 50 mV s^{-1}. (b) voltammograms of the as-prepared catalysts in 0.1 M $HClO_4$ + 2.0 M CH_3OH between 0.0 V and 0.6 V. (c) comparison of the specific mass activities of the as-prepared catalysts at 0.6 V. (d) comparison of the current density for the MOR at 0.6 V forthe as-prepared electrocatalysts before and after stability test.

Table 1
Electrocatalytic properties of the catalysts for methanol electrooxidation reaction.

Catalysts for MOR	Forward peak potential(V vs. Ag/AgCl)	Max. Specific current density(A $g^{-1}{}_{Pt}$)	I_f/I_b	Ref.
Au@Pt nanocolloids[a]	~0.66	116	~1	[37]
Pt-on-Pd nanodendrites[a]	~7	490	~1.08	[38]
FePtPd nanowires[b]	0.614	488.7	~1.05	[39]
PtPd/C hollow sphere[b]	~0.6	~510	0.85	[40]
PtPd/TP-BNGN[b]	~0.75	647.2	1.25	[41]
PtPd/C nanowire[b]	~0.6	526.1	<1	[42]
Pd-Pt concave nanocubes[b]	~0.54	~520	1.4	[43]
PtRu/PEI-CNTs[b]	~0.66	635	<1	[44]
Cubic Pd@Pt[a]	0.6	580	1.12	In this study

[a] Pt-based electorcatlaysts with a core–shell structure.
[b] Pt-based electrocatalysts with an alloy structure.

shows the relatively negative shifts compared to the Pt-based catalysts reported in other groups [37–39,41,44]. Furthermore, in the present study, the order of the forward peak potential of the as-prepared catalysts is as follows: cubic Pd@Pt (0.60 V) < cubic Pt (0.67 V) < commercial Pt (0.86 V). The negative shift of the forward anodic peak implies that the methanol electrooxidation is much easier on the shape-controlled Pt-based catalyst than that on the pure polycrystalline Pt [45]. The improved electrocatalytic properties of the cubic Pd@Pt electrocatalyst might be attributed to an excellent electrocatalytic activity of {100} facets in Pt-based NPs and the downshift of the d-band center of the Pt electronic structure, which is induced by an electronic interaction between the Pd core and the Pt shell [46]. Also, the cubic Pd@Pt electrocatalyst shows a higher maximum specific current density and/or I_f/I_b ratio, in comparison with the Pt-based electrocatalysts containing core–shell or alloy structures [37–40,42–44]. Furthermore, to evaluate the electrocatalytic stability for MOR and FAOR, the as-prepared electrocatalysts were maintained at 0.45 V for 7200 s in 0.1 M $HClO_4$ + 2.0 M CH_3OH at 25 °C, as shown in Fig. S2. The cubic Pd@Pt and cubic Pt electrocatalysts exhibited much higher retention of ~90% and 93%, respectively, at 0.6 V after the stability test, as shown in Fig. 8(d), compared to the commercial Pt. Thus, the excellent specific mass activity and electrochemical stability of the cubic Pd@Pt electrocatalyst for the methanol electrooxidation reaction may be due to the reduced amount of Pt and homogeneous Pt deposition on the Pd surface with exposed {100} facets.

4. Conclusions

We prepared the shape-controlled Pd@Pt core–shell NPs using a seeding method. The cubic Pd NPs as a core material were synthesized by selective binding of the Br^- ion in the presence of PVP in a polyol process. The cubic Pd@Pt core–shell NPs were prepared by a heterogeneous nucleation process on the cubic Pd NPs. The as-prepared Pd@Pt core–shell NPs consist of a well-defined core–shell structure with Pd core and Pt shell, cubic shape exposed {100} facets, ~97% yield, and approximately 2.5 nm thickness of the Pt shell. Furthermore, we found remarkably improved electrochemical properties of the cubic Pd@Pt electrocatalyst, such as improved specific mass current density, high I_f/I_b ratio, more negative potential of the forward peak, and superior electrochemical stability for the methanol electrooxidation in comparison with the pure cubic Pt and commercial Pt electrocatalysts. Thus, the cubic Pd@Pt electrocatalyst may be utilized as a promising anode in DMFCs.

Acknowledgements

This work was supported by the International Collaborative Energy Technology R&D Program of the Korea Institute of Energy Technology Evaluation and Planning (KETEP), granted financial resource from the Ministry of Trade, Industry & Energy, Republic of Korea. (No. 20148520120160).

Appendix A. Supplementary data

Supplementary data associated with this article can be found, in the online version, at http://dx.doi.org/10.1016/j.apcatb.2015.05.029

References

[1] E. Antolini, App. Catal. B-Environ. 74 (2007) 337–350.
[2] X. Li, A. Faghri, J. Power Sources 226 (2013) 223–240.
[3] J.N. Tiwari, R.N. Tiwari, G. Singh, K.S. Kim, Nano Energy 2 (2013) 553–578.
[4] E. Antolini, J.R.C. Salgado, E.R. Gonzalez, Appl. Catal. B-Environ. 63 (2006) 137–149.
[5] A. Hamnett, Catal. Today 38 (1997) 445–457.
[6] C. He, H.R. Kunz, J.M. Fenton, J. Electrochem. Soc. 144 (1997) 970–979.
[7] H. You, F. Zhang, Z. Liu, J. Fang, ACS Catal. 4 (2014) 2829–2835.
[8] W. Li, X. Wang, Z. Chen, M. Waje, Y. Yan, J. Phys. Chem. B 110 (2006) 15353–15358.
[9] J. Wu, J. Zhu, M. Zhou, Y. Hou, S. Gao, CrystEngComm. 14 (2012) 7572–7575.
[10] Y. Qi, T. Bian, S.-I. Choi, Y. Jiang, C. Jin, M. Fu, H. Zhang, D. Yang, Chem. Commun. 50 (2014) 560–562.
[11] L. Wang, Y. Yamauchi, Chem. Mater. 23 (2011) 2457–2465.
[12] H. Zhang, M. Jin, H. Liu, J. Wang, M.J. Kim, D. Yang, Z. Xie, J. Liu, Y. Xia, ACS Nano 5 (2011) 8212–8222.
[13] S. Guo, S. Zhang, S. Sun, Angew. Chem. Int. Ed. 52 (2013) 8526–8544.
[14] E. Herrero, K. Franaszczuk, A. Wieckowski, J. Phys. Chem. 98 (1994) 5074–5083.
[15] Y.-W. Lee, S.-B. Han, D.-Y. Kim, K.-W. Park, Chem. Commun. 47 (2011) 6296–6298.
[16] C. Kim, H. Lee, Catal. Commun. 11 (2009) 7–10.
[17] Z. Peng, H.J. You, J. Wu, H. Yang, Nano Lett. 10 (2010) 1492–1496.
[18] D. Xu, Z. Liu, H. Yang, Q. Liu, J. Zhang, J. Fang, S. Zou, K. Sun, Angew. Chem. Int. Ed. 48 (2009) 4217–4221.
[19] G. Wang, M.A. Van Hove, P.N. Ross, M.I. Baskes, J. Phys. Chem. B 109 (2005) 11683–11692.
[20] S.R. Brankovic, J.X. Wang, R.R. Adžić, Electrochem. Solid State Lett. 4 (2001) A217–A220.
[21] B. Lim, M. Jiang, P.H.C. Camargo, E.C. Cho, J. Tao, X. Lu, Y. Zhu, Y. Xia, Science 324 (2009) 1302–1305.
[22] S. Wang, N. Kristian, S. Jiang, X. Wang, Nanotechnology 20 (2009) 025605.
[23] J.X. Wang, H. Inada, L. Wu, Y. Zhu, Y.M. Choi, P. Liu, W.-P. Zhou, R.R. Adzic, J. Am. Chem. Soc. 131 (2009) 17298–17302.
[24] L. Kuai, S. Wang, B. Geng, Chem. Commun. 47 (2011) 6093–6095.
[25] J. Zhang, J. Fang, J. Am. Chem. Soc. 131 (2009) 18543–18547.
[26] M. Tsuji, N. Miyamae, S. Lim, K. Kimura, X. Zhang, S. Hikino, M. Nishio, Cryst. Growth Des. 6 (2006) 1801–1807.
[27] N.V. Long, T. Asaka, T. Matsubara, M. Nogami, Acta Mater. 59 (2011) 2901–2907.
[28] H.-C. Peng, S. Xie, J. Park, X. Xia, Y. Xia, J. Am. Chem. Soc. 135 (2013) 3780–3783.
[29] H. Zhang, M. Jin, Y. Xiong, B. Lim, Y. Xia, Acc. Chem. Res. 46 (2013) 1783–1794.
[30] B. Lim, M. Jiang, J. Tao, P.H.C. Camargo, Y. Zhu, Y. Xia, Adv. Funct. Mater. 19 (2009) 189–200.
[31] B. Lim, H. Kobayashi, T. Yu, J. Wang, M.J. Kim, K.-Y. Li, M. Rycenga, Y. Xia, J. Am. Chem. Soc. 132 (2010) 2506–2507.
[32] G. Fu, Z. Liu, Y. Chen, J. Lin, Y. Tang, T. Lu, Nano Research 7 (2014) 1205–1214.
[33] D. Wang, H.L. Xin, Y. Yu, H. Wang, E. Rus, D.A. Muller, H.D. Abruña, J. Am. Chem. Soc. 132 (2010) 17664–17666.
[34] N.M. Markovic, H.A. Gasteiger, P.N. Ross Jr., J. Phys. Chem. 99 (1995) 3411–3415.
[35] C. Wang, H. Daimon, T. Onodera, T. Koda, S. Sun, Angew. Chem. Int. Ed. 47 (2008) 3588–3591.
[36] R. Manohara, J.B. Goodenough, J. Mater. Chem. 2 (1992) 875.
[37] H. Ataee-Esfahani, L. Wang, Y. Nemoto, Y. Yamauchi, Chem. Mater. 22 (2010) 6310–6318.
[38] L. Wang, Y. Nemoto, Y. Yamauchi, J. Am. Chem. Soc. 133 (2011) 9674–9677.
[39] S. Guo, S. Zhang, X. Sun, S. Sun, J. Am. Chem. Soc. 133 (2011) 15354–15357.
[40] Y.-Y. Chu, Z.-B. Wang, Z.-Z. Jiang, D.-M. Gu, G.-P. Yin, J. Power Sources 203 (2012) 17–25.
[41] S. Guo, S. Dong, E. Wang, ACS Nano 4 (2010) 547–555.
[42] Y.-Y. Chu, Z.-B. Wang, J. Cao, D.-M. Gu, G.-P. Yin, Fuel Cells 13 (2013) 380–386.
[43] F. Zhan, T. Bian, W. Zhao, H. Zhang, M. Jin, D. Yang, CrystEngComm. 16 (2014) 2411–2416.
[44] Y. Cheng, C. Xu, P.K. Shen, S.P. Jiang, Appl. Catal. B-Environ. 158–159 (2014) 140–149.
[45] Z. He, J. Chen, D. Liu, H. Zhou, Y. Kuang, Diamond Relat. Mater. 13 (2004) 1764–1770.
[46] X. Liu, G. Xu, Y. Chen, T. Lu, Y. Tang, W. Xing, Sci. Rep. 5 (2015) 7619.